International Journal of Mining Science and Technology 36 (2026) 903–915

Contents lists available at ScienceDirect

International Journal of Mining Science and Technology

journal homepage: www.elsevier.com/locate/ijmst

Boosting electrochemical reduction-recovery of trace gold(I) with ferric-modified walnut shell charcoal

Shaoxian Song [a], Weiquan Zhan [a,b,*], Qizheng Weng [a], Chun Zhan [c], Feifei Jia [a,b,*]

[a] Key Laboratory of Green Utilization of Critical Non-metallic Mineral Resources of Ministry of Education, Wuhan University of Technology, Wuhan 430070, China
[b] School of Resources and Environmental Engineering, Wuhan University of Technology, Wuhan 430070, China
[c] Department of Energy Storage Science and Engineering, School of Metallurgical and Ecological Engineering, University of Science and Technology Beijing, Beijing 100083, China

ARTICLE INFO

Article history:
Received 15 December 2025
Received in revised form 26 January 2026
Accepted 6 February 2026
Available online 20 February 2026

Keywords:
Trace gold(I) recovery
Thiosulfate leaching
Electrochemical reduction-recovery
Ferric modification
$Fe_2(SO_4)_3$-WSC electrodes

ABSTRACT

Enhancing the electrochemical reduction-recovery of trace-level gold(I) in thiosulfate media is essential for advancing environmentally friendly, cyanide-free hydrometallurgical technologies. In this work, walnut shell charcoal (WSC) was modified using various ferric compounds to enhance its performance as an electrode. Ferric modification led to stable surface coating which significantly improved electrical conductivity and electrochemical behavior by increasing the specific capacitance and reducing the charge transfer resistance during gold(I) recovery. Among the different ferric precursors tested, ferric sulfate ($Fe_2(SO_4)_3$) modification exhibited the most outstanding performance, increasing the reduction capacity from 36.52 mg/g (pristine WSC) to 97.70 mg/g, a 2.67-fold enhancement. Under optimized electrochemical conditions, this modified electrode achieved a 95.72% recovery for trace gold(I) (5 mg/L), significantly outperforming electrodes modified with $FeCl_3$. Systematic experiments and material characterizations revealed that $Fe_2(SO_4)_3$ modification led to the formation of surface-bound sulfate groups and oxygen-rich functional sites, which enhance the adsorption affinity toward gold species and facilitated preconcentration near active centers. Moreover, density functional theory (DFT) simulations confirmed strong interactions between sulfur-derived oxygen atoms and gold(I), contributing to the improved recovery. Chloride from ferric chloride also showed ability to coordinate with oxygen atoms, contributing to a moderate recovery. These results collectively highlight the importance of ferric source selection in optimizing carbon-based electrodes for noble metal recovery, providing a promising strategy for sustainable hydrometallurgical processes.

1. Introduction

Gold is a valuable metal primarily extracted from ores and electronic waste [1,2]. Hydrometallurgical processes [3,4] are commonly employed to dissolve gold from solid phases into aqueous solutions. Among these methods, cyanide leaching is widely used in industrial applications [5,6]. However, the high toxicity of cyanide [7,8] poses significant environmental and safety concerns. Therefore, the development of environmentally friendly and sustainable leaching methods is an urgent priority. Thiosulfate leaching [9–11] has emerged as one of the most promising alternatives due to its non-toxic nature and rapid leaching kinetics. Nevertheless, a major challenge hindering its widespread applications is the efficient recovery of gold from low-concentration solutions [12,13]. In practical industrial scenarios, such as the processing of refractory gold ores or the recycling of electronic waste, gold concentrations in the leaching solutions or residual streams can be significantly dilute. For instance, residual concentrations of invisible gold in pyrite and arsenopyrite grain centers are often less than 1–5 mg/L [14]. Addressing this issue is crucial for advancing the practical implementation of thiosulfate-based gold extraction technologies.

To date, various conventional methods, including ion exchange [15,16], precipitation [17], adsorption [18–20], and electrodeposition [21], have encountered challenges such as weak interactions with $Au(S_2O_3)_2^{3-}$, poor material stability, high costs, and low recovery. In a previous work, an electrochemical reduction-recovery approach [22,23] was proposed for recovering $Au(S_2O_3)_2^{3-}$. This method not only enables the efficient recovery of gold(I) but also facilitates their direct reduction to elemental gold. This approach has the potential to streamline industrial gold recovery processes by reducing the required treatment steps.

* Corresponding authors.
E-mail addresses: zhan_weiquan@163.com (W. Zhan), feifeijia@whut.edu.cn (F. Jia).

https://doi.org/10.1016/j.ijmst.2026.02.005
2095-2686/

Among the electrode materials used, carbon electrodes [24,25] have advantages such as low cost and high specific surface area, making them effective for recovering gold(I). Through appropriate thermal and chemical treatments, walnut shells [26] can be transformed into biochar materials exhibiting favorable adsorption performance. Due to their wide availability and cost-effectiveness, walnut shells serve as an abundant raw material for biochar production, particularly in China [27,28]. Previous research [29] has demonstrated that this electrode material owned efficient gold(I) recovery to a certain extent, with the primary active sites originating from its instinct nature.

To further enhance the gold(I) recovery performance of walnut shell charcoal (WSC) electrodes, surface modification [30–32] is a crucial strategy to optimize the interactions between electrodes and targeted ions. Among various transition metals, iron (Fe) stands out as a superior modification reagent due to its excellent biocompatibility and environmental friendliness, aligning with the goals of green hydrometallurgy. Unlike copper, which tends to react with thiosulfate to form precipitates or consume leaching reagents, iron species can be stably anchored onto the carbon surface through Fe—C bonds or Fe—O species [33,34]. Crucially, the performance of iron-modified carbon is not solely dependent on the Fe cation itself, but is significantly governed by the synergistic effect between iron and its coordinated ligands (such as sulfur, chloride, or oxygen groups). While previous studies have explored iron-containing adsorbents for general pollutant removal [35,36], the comparative influence of different ferric precursors on the electrochemical reduction-recovery of trace gold(I) remains poorly understood.

In this work, we systematically investigate a series of Fe (III)-containing precursors ($Fe_2(SO_4)_3$, $FeCl_3$, and $Fe(NO_3)_3$) to modify WSC. We aim to elucidate how different anion-coordinated environments dictate the adsorption affinity and charge transfer resistance during the gold(I) recovery process. By combining experimental optimization with DFT simulations, this study reveals the unique mechanism of sulfate-mediated preconcentration, providing a novel strategy for high-efficiency noble metal recovery.

2. Materials and methods

2.1. Reagents

A stock solution of chloroauric acid ($HAuCl_4$, 1000 mg/L) was procured from Well Group Scientific Ltd., USA. Ammonium thiosulfate ($(NH_4)_2S_2O_3$) was sourced from Sigma-Aldrich (Shanghai, China). Vinylidene fluoride ($F_2H_2F_2$) was supplied by Alfa Aesar (China). Conductive carbon black was provided by Suzhou Sinero Technology Co., Ltd. (China). All other analytical-grade reagents were obtained from Sinopharm Chemical Reagent Co., Ltd. (Shanghai, China) and used as received. Ultrapure water with a resistivity of 18.2 MΩ·cm was generated using a Millipore purification system (France).

2.2. Preparation of WSC materials

The preparation of WSC followed the procedure outlined in the previous work [29]. First, walnut shells were ground into fine powder using a pulverizer, followed by sieving to obtain the desired particle size. The sieved product was then placed in an alumina boat and subjected to pyrolysis in a tube furnace under a nitrogen atmosphere at a specific temperature for 60 min. After cooling, the obtained carbonized material was dispersed in an ethanol solution under stirring, then washed multiple times with deionized water. Finally, the sample was freeze-dried to obtain the WSC. The synthesized products were designed as WSC_X, where X represents the carbonization temperature.

2.3. Preparation of Fe (III)-WSC materials

The modify WSC with $Fe_2(SO_4)_3$, the obtained WSC samples were immersed in an $Fe_2(SO_4)_3$ solution at a solid-to-liquid ratio of 10:1. The mixture was subjected to ultrasonic treatment at 30 °C for 2.5 h. After modification, the products were repeatedly rinsed with ultrapure water to remove residual species, followed by drying at 110 °C for 12 h. The obtained samples were denoted as $(Fe_2(SO_4)_3)_Y$-WSC, where Y represents the concentration of $Fe_2(SO_4)_3$.

To investigate the effect of different ferric sources, the same modification procedure was applied using alternative ferric precursors, such as $FeCl_3$ and Fe $(NO_3)_3$. The corresponding modified materials were denoted as $FeCl_3$-WSC and Fe $(NO_3)_3$-WSC, respectively.

2.4. Electrodes fabrication

Electrodes were fabricated by coating titanium plate as before [37]. Titanium plates were selected as the conductive substrate owing to its excellent stability and resistance to strong acids and alkalis. The as-prepared material was blended with conductive carbon black and polyvinylidene fluoride as a mass ratio of 8:1:1, and manually ground to obtain homogeneous electrode slurry. The mixture was then dissolved in dimethylacetamide solvent to form a homogeneous slurry. A titanium plate was selected as the substrate for coating. The coated electrode was then placed in an oven at 60 °C and heated for at least 60 min. After drying, the electrode was immersed in deionized water for 12 h to remove residual solvents, followed by an additional drying step at 60 °C for 6 h before use.

2.5. Electrochemical reduction-recovery of gold(I)

The $Au(S_2O_3)_2^{3-}$ complex solution was prepared by reacting $HAuCl_4$ with $Na_2S_2O_3$ in deionized water. A molar excess of thiosulfate (Au: $S_2O_3^{2-}$ = 1:4) was employed, where $S_2O_3^{2-}$ acts as both a reducing agent and a complexing ligand. To ensure stability, the pH was adjusted to 10.0 using NaOH to confirm $Au(S_2O_3)_2^{3-}$ is the predominant species under these alkaline and reductive conditions [38,39]. Subsequently, the prepared electrodes were immersed in an electrolytic cell containing the $Au(S_2O_3)_2^{3-}$ solution. The cell was connected to a peristaltic pump operating at 50 r/min to ensure continuous circulation. At selected time points, aliquots (2.5 mL) were withdrawn, filtered through a 0.22 μm membrane, and analyzed for gold concentration using atomic absorption spectroscopy (AAS).

$$R_e = \frac{(C_0 - C_t) \times (V_0 - V_t)}{m} \quad (1)$$

$$R_e = \frac{(C_0 - C_t)}{C_0} \times 100\% \quad (2)$$

where C_0 and C_t refer to the gold concentration at the initial time and at time t, respectively, mg/L; V_0 and V_t the solution volumes at the same time points, L; and m the mass of the coating material, mg.

2.6. Electrochemical characterization

Electrochemical impedance spectroscopy (EIS), cyclic voltammetry (CV), and linear sweep voltammetry (LSV) were performed on a VersaSTAT-450 using a conventional three-electrode

configuration, in which a platinum served as the counter electrode. The reference electrode was a Hg/HgO electrode (1 M KOH). The working electrode consisted of a titanium plate (1 cm^2) with a single-sided material coating. The electrochemical tests were performed in two different electrolyte solutions, 1 M Na_2SO_4 solution and 5 mg/L $Au(S_2O_3)_2^{3-}$ solution. For EIS measurements, the frequency ranged from 0.01 Hz to 10,000 Hz. The EIS data was fitted with an equivalent circuit. The charge transfer resistance was specifically monitored to evaluate the electrochemical activity of various modified electrodes toward gold(I) reduction.

2.7. Contact angle tests

A 1 g sample of prepared materials was compressed into a disc under a pressure of 18 MPa. The contact angle of the materials subsequently measured using a JC2000DM contact angle measurement system.

2.8. Material characterizations

Phase structures were identified by X-ray diffractometer (D8 Advance, Bruker AXS, Germany) using CuKα radiation. Surface functional groups of the materials were characterized using an FTIR spectrometer (Nicolet 6700, Thermo Scientific, USA) over a range of 4000–400 cm^{-1}. Microstructural morphology was conducted using a Phenom ProX G6 SEM (Netherlands) and an FEI Tecnai G2 F20 field-emission TEM (USA). Elemental chemical states were analyzed by XPS spectroscopy (*k*-Alpha, Thermo Scientific, USA). The gold and ferric concentrations in the filtrate were measured using an Agilent 280AA spectrometer (G8434A, USA).

2.9. DFT calculations

The interactions between gold(I) and different ferric compounds were investigated using DFT calculations performed with the CASTEP module. Generalized gradient approximation (GGA) with PW91 exchange–correlation functional was employed. Calculations were conducted under periodic boundary conditions using a cubic supercell with dimensions of 20 × 20 × 20 $Å^3$, providing sufficient vacuum space to eliminate periodic interactions. A plane-wave cutoff energy of 370 eV was applied. The self-consistent field (SCF) procedure utilized the Pulay density mixing method to achieve convergence.

3. Results and discussion

3.1. Microstructure and chemical compositions

Various WSC prepared at different synthesized temperatures were all modified by $Fe_2(SO_4)_3$ to reveal the role of modification inside. Phase structures of $Fe_2(SO_4)_3$-WSC after multi-times washing were characterized by X-ray diffraction (XRD) in Fig. 1. The peaks located at ~25° and 43° in all the prepared materials are originated from the characteristic amorphous structure of carbon, while others at ~13°, 19°, 25°, 26°, 27°, 29°, 36°, 38°, 39° respectively represented (1 0 1), (0 1 2), (2 1 1), (−2 0 2), (−1 1 3), (1 2 2), (3 1 1), (−2 0 4), (2 3 1) of $Fe_2(SO_4)_3$ (JCPDS 71-0148)[40], which demonstrates the successful modification on WSC using $Fe_2(SO_4)_3$.

To analyze the chemical composition of $Fe_2(SO_4)_3$-WSC, XPS was performed. Fig. S1 presented the full-spectrum XPS scan, where distinct absorption peaks are observed at binding energies of ~712.9, 532.1, 407.8, 285.2, and 169.2 eV, corresponding to Fe 2*p*, O 1*s*, N 1*s*, C 1*s*, and S 2*p*, respectively. This indicates that the $Fe_2(SO_4)_3$-WSC is primarily composed of these elements. Fig. 2a displays the high-resolution C 1*s* spectrum, where peaks at ~292.3, 285.8, and 284.3 eV corresponded to C==O, C—O, and C—C bonds, respectively, which originates from the common functions in carbon materials [41]. The O 1*s* spectrum in Fig. 2b exhibits a peak at ~531.1 eV, which is attributed to C—O bonding [42]. In the S 2*p* spectrum (Fig. 2c), the peaks at ~169.1 and 168.0 eV corresponded to S $2p_{1/2}$ and S $2p_{3/2}$ of $Fe_2(SO_4)_3$, respectively [43]. Finally, Fig. 2d presents the Fe 2*p* spectrum of $Fe_2(SO_4)_3$-WSC, revealing that Fe primarily exists in the trivalent oxidation state (Fe^{3+}), and part in divalent Fe (Fe^{2+}), which originates from the $Fe_2(SO_4)_3$ [44]. The presence of additional peaks confirms the existence of Fe–O bonds, indicating that Fe likely interacted with O [45] in the WSC. The XPS analysis results were consistent with those from XRD, confirming successful modification of WSC with $Fe_2(SO_4)_3$.

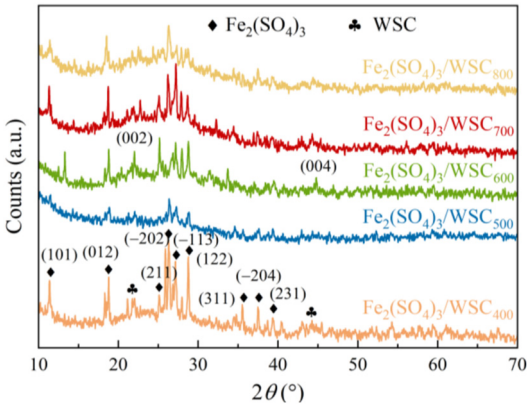

Fig. 1. XRD patterns of $Fe_2(SO_4)_3$-WSC prepared at different synthesized temperatures.

3.2. Morphology and elemental states

To investigate the morphology of $Fe_2(SO_4)_3$-WSC, scanning electron microscope (SEM) was applied. Before modification, the surface (Fig. 3a) appears relatively smooth with larger, more compact structures. After modification, the surface of $Fe_2(SO_4)_3$-WSC (Fig. 3b) become rougher and more porous, with fine granular structures distributed across the material, indicating successful modification. The embedded EDS pattern confirms that the surface of WSC is primarily composited of C element. After $Fe_2(SO_4)_3$ modification, O, Fe, and S elements are uniformly distributed across the surface of the WSC, while the C content is relatively lower. This indicates that the surface modification with $Fe_2(SO_4)_3$ is predominant.

With the aim of revealing the further microstructure on $Fe_2(SO_4)_3$-WSC morphology, high-resolution transition electron microscope (HRTEM) was used. In Fig. 4, $Fe_2(SO_4)_3$-WSC exhibits distinct morphological structures, including the presence of crystalline structure. Meanwhile, a lattice spacing of ~0.6 nm interlayer spacing is detected, suggesting a layered water-retaining structure rather than pure anhydrous $Fe_2(SO_4)_3$.

3.3. Electrochemical reduction-recovery of gold(I) by $Fe_2(SO_4)_3$-WSC

Electrochemical reduction-recovery performances of gold(I) by $Fe_2(SO_4)_3$-WSC were carried out, illustrated in Fig. 5. It is observed that the reduction capacity (Fig. 5a) of $Fe_2(SO_4)_3$-WSC electrodes increases substantially, generally ranging from 1.5 to 2.0 times higher than that of the unmodified WSC electrodes. Except reduction capacity, WSC_{400} electrodes achieved a recovery of only 69.9%, after modification, $Fe_2(SO_4)_3$-WSC_{400} electrodes exhibits significant

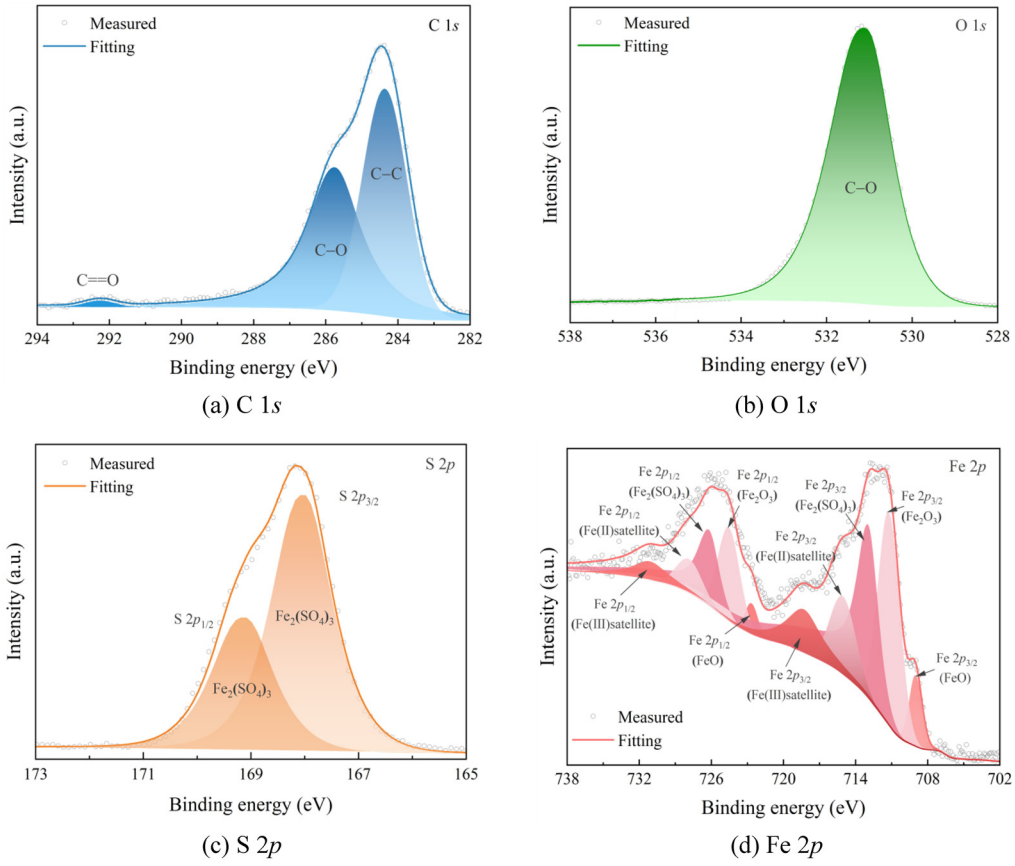

Fig. 2. XPS high-resolution spectra of $Fe_2(SO_4)_3$-WSC.

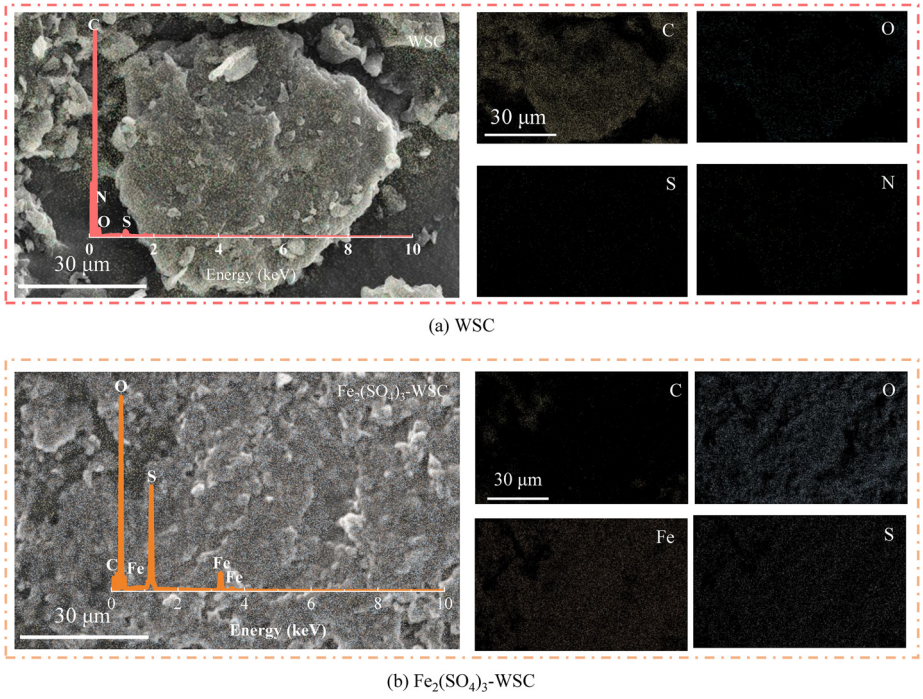

Fig. 3. SEM images and corresponding EDS mappings of WSC and $Fe_2(SO_4)_3$-WSC.

improvements (increased to 82.8%) (Fig. 5b). Moreover, all $Fe_2(SO_4)_3$ modified WSC electrodes shows an increased recovery compared with WSC electrodes without modification. Among them, WSC carbonized at 500 °C (whether modified or not) exhibited the highest gold(I) recovery performance, which is consistent with the previous findings [29]. This optimal performance at

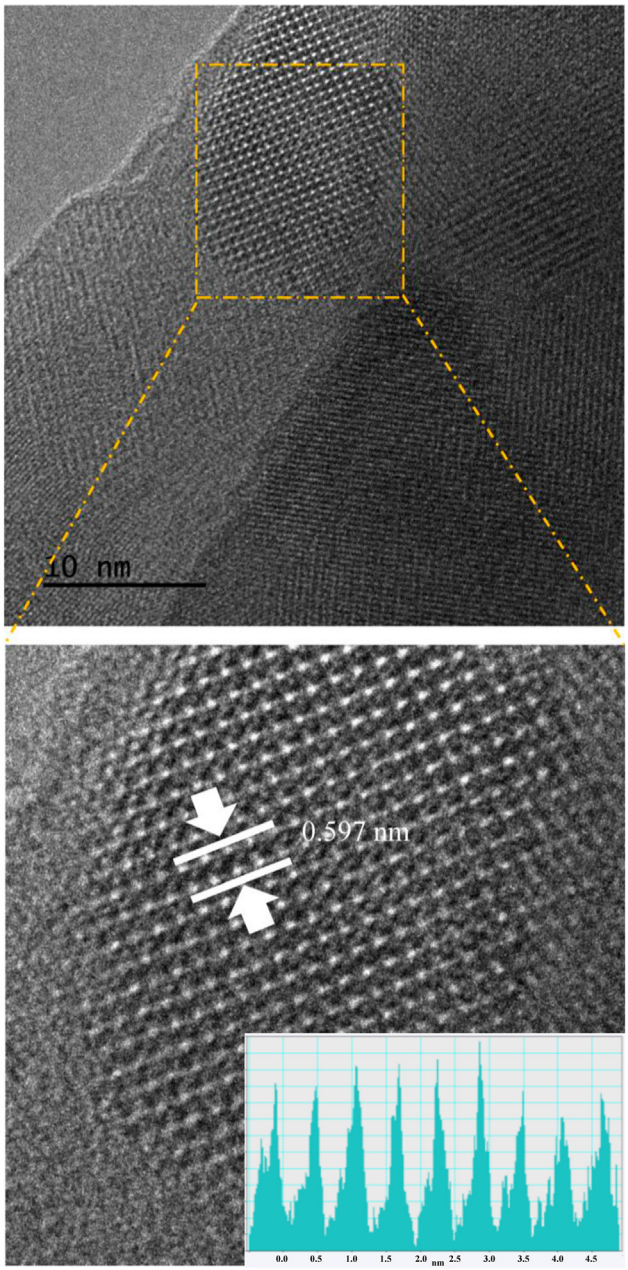

Fig. 4. HRTEM images of $Fe_2(SO_4)_3$-WSC.

500 °C is primarily attributed to the balance between surface chemistry and structural integrity. It can be concluded that the $Fe_2(SO_4)_3$ modification method is applicable to WSC at different temperatures.

Fig. 6a presents the electrochemical reduction-recovery performances of $Fe_2(SO_4)_3$-WSC for gold(I) at different initial concentrations. As observed from the results, the $Fe_2(SO_4)_3$-WSC exhibits a stable and efficient electrochemical reduction-recovery effect across the concentration range of 1–10 mg/L. Besides, the reduction capacity and recovery increase with the initial gold(I) concentration, confirming the material's strong potential for practical applications. The effect of different pH values on the electrochemical reduction-recovery of gold(I) was investigated (Fig. 6b). The electrochemical reduction-recovery performance of gold(I) is optimized within the pH range of 8 to 10. However, when the pH exceeds 10, the reduction capacity and recovery decline. One possible reason is that at higher pH levels, OH^- in the solution competes with $Au(S_2O_3)_2^{3-}$ for active sites on the $Fe_2(SO_4)_3$-WSC electrodes [29]. Additionally, excessive pH adversely affects the modified WSC itself, further reducing the electrochemical reduction-recovery efficiency of gold(I).

Subsequently, we examined the influence of operational parameters on the electrochemical reduction-recovery of gold(I). Fig. 6c presents the electrochemical reduction-recovery performances of gold(I) using $Fe_2(SO_4)_3$-WSC electrodes at different electrode spacings. Both the recovery and reduction capacity exhibited at initial increase followed by a decline. When the electrode spacing was 2 nm, the recovery reached 92.3%. At 5 mm, both recovery and reduction capacity peaked at 96.1% and 119.1 mg/g, respectively. This phenomenon is primarily attributed to the extended migration path of $Au(S_2O_3)_2^{3-}$ and the increased resistance of the electrolyte. This reduced driving force, coupled with increased internal resistance, slows down the migration rate of $Au(S_2O_3)_2^{3-}$ toward the electrode surface, thereby leading to decreased. Further, the effect of applied voltage on electrochemical reduction-recovery performance of gold(I) using $Fe_2(SO_4)_3$-WSC electrodes is studied (Fig. 6d). Without voltage, the recovery of gold(I) remains negligible, primarily relying on slow passive adsorption. Upon the application of voltage, the migration of gold(I) within the electric field is significantly accelerated. The recovery performance increases proportionally with the voltage until reaching an optimum at 1.2 V. At this critical threshold, the driving force of electrostatic interactions effectively overcomes the steric resistance and volume repulsion within the microporous structure of electrodes. Consequently, ions begin to accumulate rapidly within the pores, inducing the formation of surface charges on the internal pores. These enhanced surface charges create a positive feedback loop, attracting a greater density of gold(I) into the active sites, thereby maximizing the recovery capacity. However, when the voltage was further increased to 1.6 V, the occurrence of side reactions, particularly water electrolysis, lead to an increased ion concentration, resulting in a slight decrease in recovery performances.

3.4. Microstructure of $Fe_2(SO_4)_3$-WSC after gold(I) recovery

TEM analysis was conducted to investigate the morphology of $Fe_2(SO_4)_3$-WSC electrodes after the electrochemical reduction-recovery of gold(I). As observed in Fig. 7, small particles are present on the surface of the recovered $Fe_2(SO_4)_3$-WSC. To further analyze the elemental composition of these particles, an EDS analysis was performed (Fig. 8). The results show that C, O, S, and Fe were uniformly distributed on the $Fe_2(SO_4)_3$-WSC's surface, while gold is exclusively found in the small particles, suggesting that they consist of the recovered gold. To confirm the structural nature of these gold particles, more TEM images and HRTEM were employed. The lattice spacing of the small particles was measured to be 0.24 nm, corresponding to the (1 1 1) crystal plane of metallic gold. This confirmed that $Au(S_2O_3)_2^{3-}$ was reduced and recovered in its metallic form on the $Fe_2(SO_4)_3$-WSC electrodes.

XPS analysis was conducted on $Fe_2(SO_4)_3$-WSC electrodes after gold(I) recovery. Fig. 9a presents the full-spectrum scan, where distinct absorption peaks are observed at binding energies of ~713.1, 531.1, 285.2, 164.7, and 88.7 eV, corresponding to Fe 2*p*, O 1*s*, C 1*s*, S 2*p* and Au 4*f*, respectively. This indicates that the primary elemental composition of $Fe_2(SO_4)_3$-WSC electrodes remains unchanged after gold(I) recovery. Additionally, the presence of gold elements detected on the recovered electrodes confirms the successful recovery of gold(I). Fig. 9b displays the C 1*s* spectrum, with peaks assigned to C==O, C—O, and H—O bonds. Similarly, Fig. 9c presents the O 1s spectrum, showing peaks corresponding to C==O, C—O, and H—O bonds. The S 2*p* (Fig. 9d) and Fe 2*p* (Fig. 9e) spectra further confirm the presence of $Fe_2(SO_4)_3$, demon-

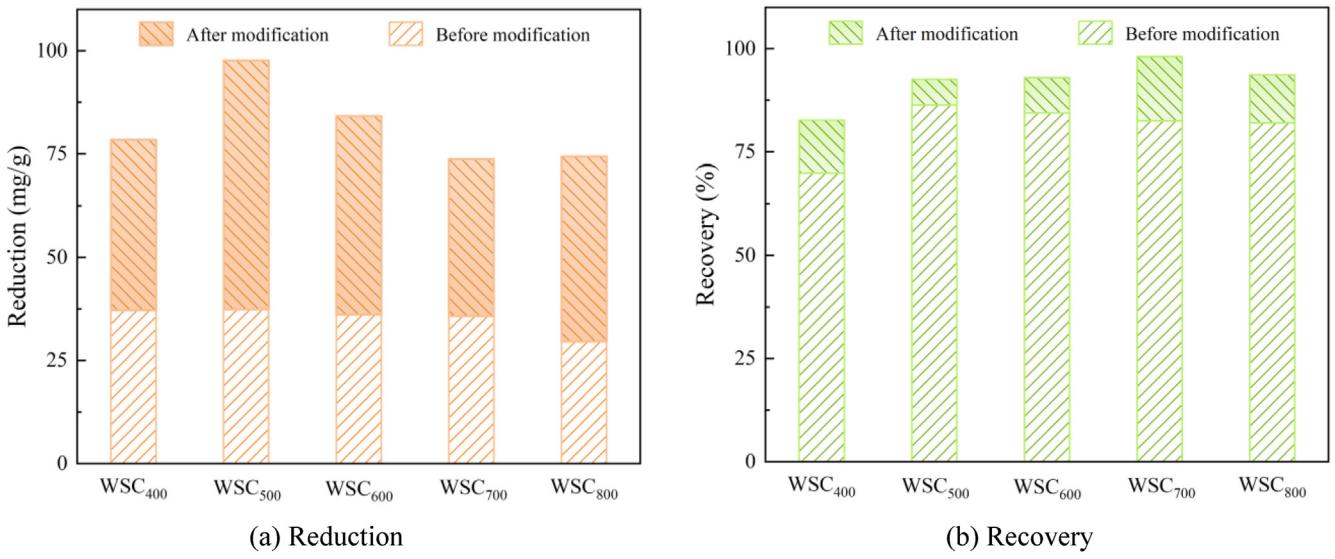

Fig. 5. Reduction capacity and recovery of gold(I) by WSC electrodes before and after $Fe_2(SO_4)_3$ modification.

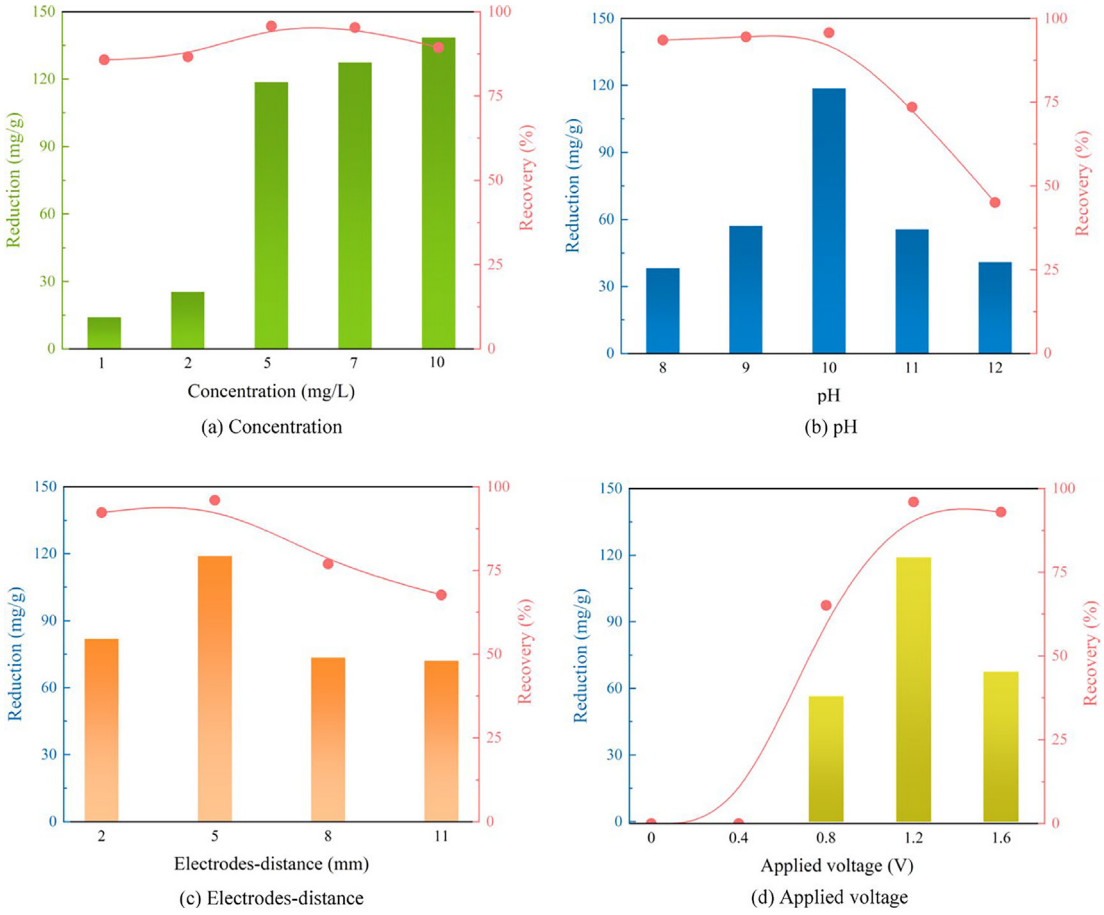

Fig. 6. Effects of initial gold(I) concentration, pH, Electrodes-distance, and applied voltage on gold(I) recovery by $Fe_2(SO_4)_3$-WSC electrodes.

strating that the elemental composition remains largely unchanged compared to its pre-reaction state. The consistency in the peaks across these spectra suggests no significant alterations occurred, indicating that the primary reduction reaction predominantly driven by the applied voltage. Fig. 9f presents the Au 4*f* spectrum, where peaks at ~87.4 and 83.8 eV correspond to metallic gold, confirming that $Au(S_2O_3)_2^{3-}$ was reduced to its metallic form during the recovery process [46]. This result aligns with the TEM findings, further demonstrating the successful electrochemical reduction of gold(I) to elemental gold.

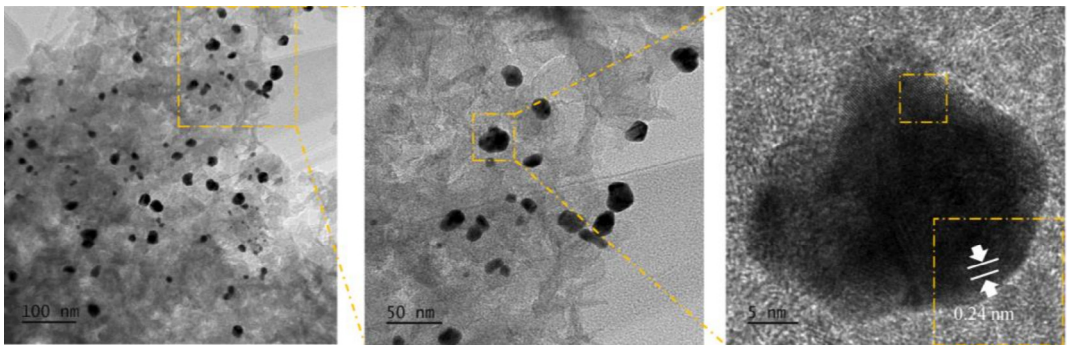

Fig. 7. TEM images of $Fe_2(SO_4)_3$-WSC electrodes after gold(I) recovery.

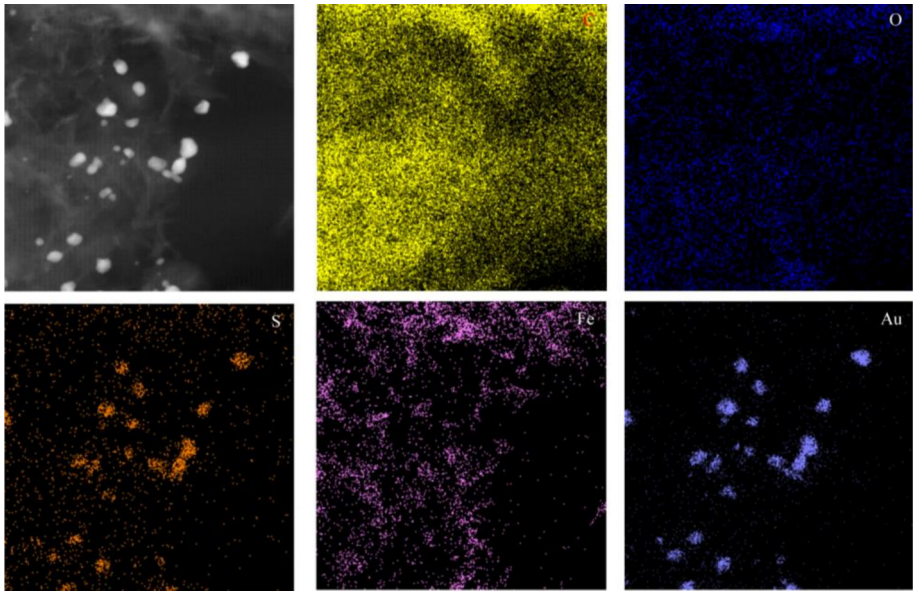

Fig. 8. TEM image and corresponding EDS mappings of $Fe_2(SO_4)_3$-WSC electrodes after gold(I) recovery.

3.5. Mechanism for improved electrochemical reduction-recovery of gold(I)

To investigate the electrochemical reduction-recovery of gold(I) using $Fe_2(SO_4)_3$-WSC electrodes, electrochemical behaviors were tested in a gold-containing solution. The CV results (Fig. 10a) reveal a reduction peak appearing between −0.6 and −0.2 V, confirming the reduction of $Au(S_2O_3)_2^{3-}$ into metallic gold. The enclosed area in CV curve is closely related to the specific capacitance and reduction performances, where a larger area indicates stronger reduction capability. It is evident that the $Fe_2(SO_4)_3$ modified WCS exhibits significantly larger specific capacitance compared to WSC, demonstrated its enhanced reduction performance. Additionally, through LSV results (Fig. S2), higher electrochemical reduction is observed after $Fe_2(SO_4)_3$ modification in WSC. EIS was employed to assess charge transfer resistance [47], where a smaller semicircle in the Nyquist plot corresponds to lower electron transfer resistance. As shown in Fig. 10b, $Fe_2(SO_4)_3$ modification enhances the electron transfer rate, facilitating the electrochemical reduction reaction.

A similar phenomenon of $Fe_2(SO_4)_3$-WSC electrodes was observed in the Na_2SO_4 solution system (Fig. 10c, d), further confirming that $Fe_2(SO_4)_3$ modification improves the electrode's electrochemical double layer capacitance (EDLC) performance, thereby strengthening its electrochemical reduction capabilities. In addition, the CV curve of $Fe_2(SO_4)_3$-WSC exhibits a more rectangular shape, indicating enhanced ion transport and adsorption capabilities. This suggests that $Fe_2(SO_4)_3$ modification improves the electrode's capacitive behaviors, facilitating more efficient electrochemical reduction-recovery of gold(I).

The contact angle is another key factor influencing the reaction rate. A smaller contact angle indicates a higher surface wettability, facilitating faster interactions between the material and hydrophilic ions. Contact angle measurements reveal that $Fe_2(SO_4)_3$-WSC (Fig. 11a) exhibited a significantly lower contact angle compared to the unmodified WSC (Fig. 11b). After 8 min, the contact angle reaches zero, indicating superior hydrophilicity, which is highly favorable for the electrochemical reduction-recovery of gold(I).

3.6. Effect of $Fe_2(SO_4)_3$ contents on gold(I) recovery

To further evaluate the impact of $Fe_2(SO_4)_3$ dosages in $Fe_2(SO_4)_3$-WSC electrodes on the gold(I) recovery performances, we systematically investigated the influence of varying $Fe_2(SO_4)_3$ dosages on the recovery performances. First, FTIR was used to analyze the functional group structures of WSC modified with varying $Fe_2(SO_4)_3$ concentrations (Fig. 12a). The vibrational peak at ~3443 cm^{-1} primarily originates from hydrogen-bonded surface –OH groups, while the peak at ~3234 cm^{-1} is likely attributed to N—H vibrations from ammonia. After modification, multiple peaks

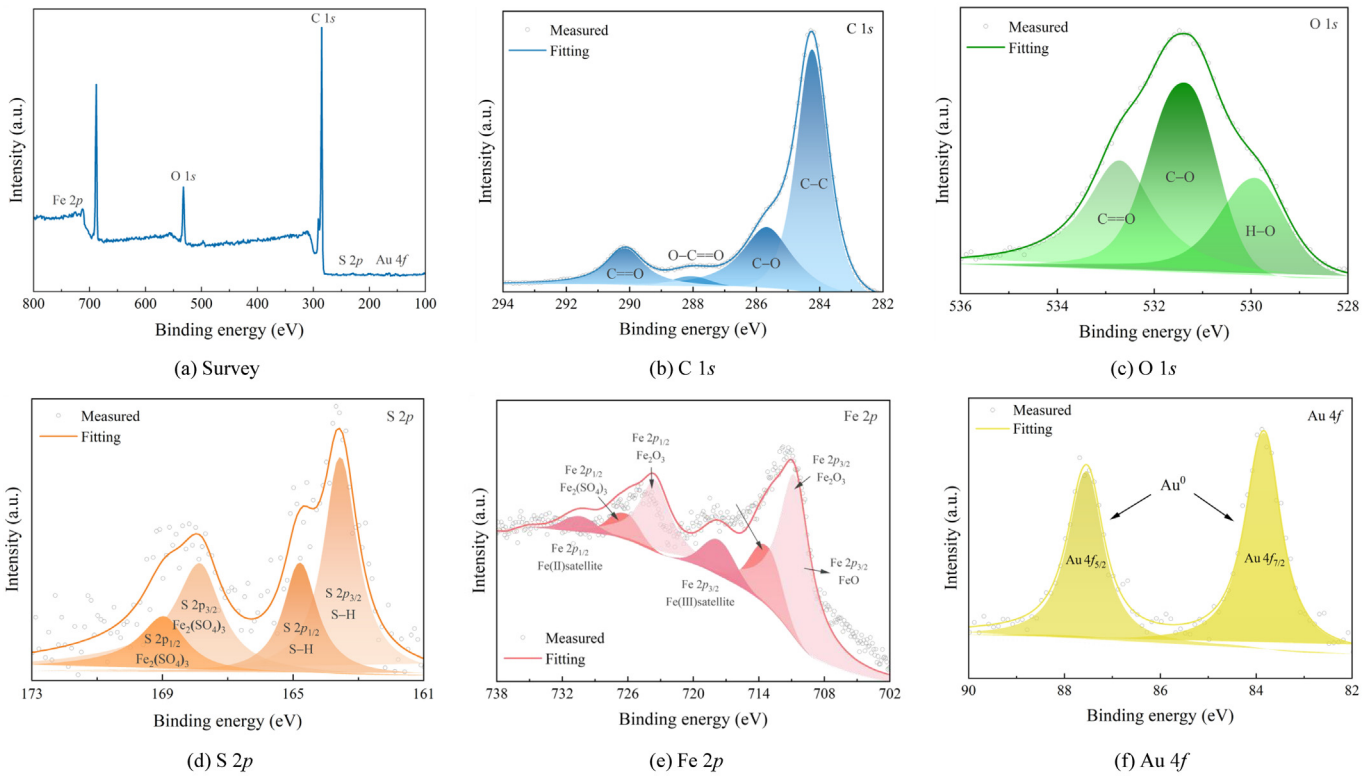

Fig. 9. XPS spectra of $Fe_2(SO_4)_3$-WSC electrodes after gold(I) recovery.

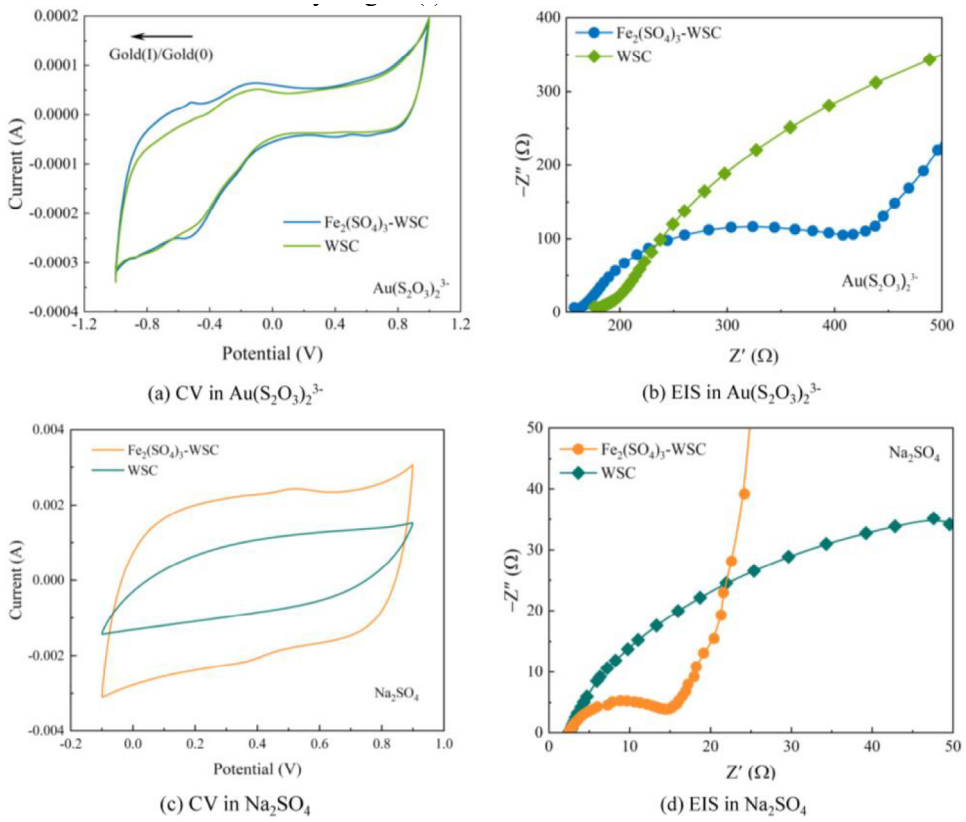

Fig. 10. CV and EIS curves of WSC electrodes with and without $Fe_2(SO_4)_3$ modification in $Au(S_2O_3)_2^{3-}$ and Na_2SO_4 solutions.

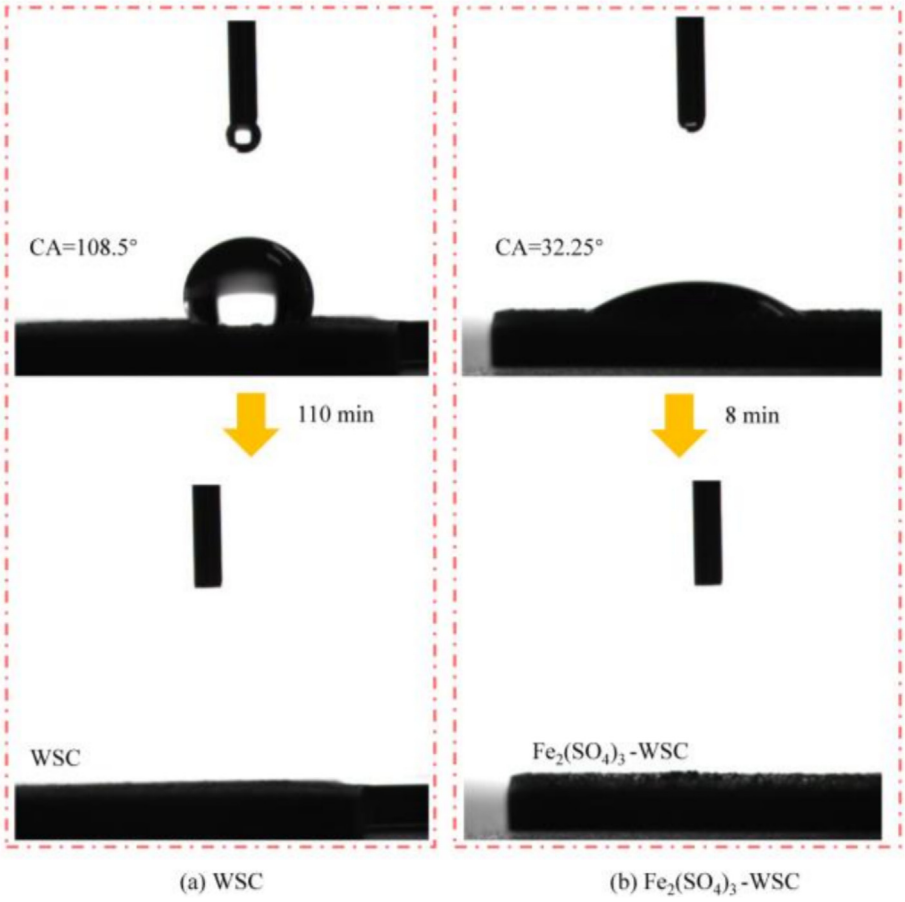

Fig. 11. Contact angles tests of WSC and $Fe_2(SO_4)_3$-WSC electrodes.

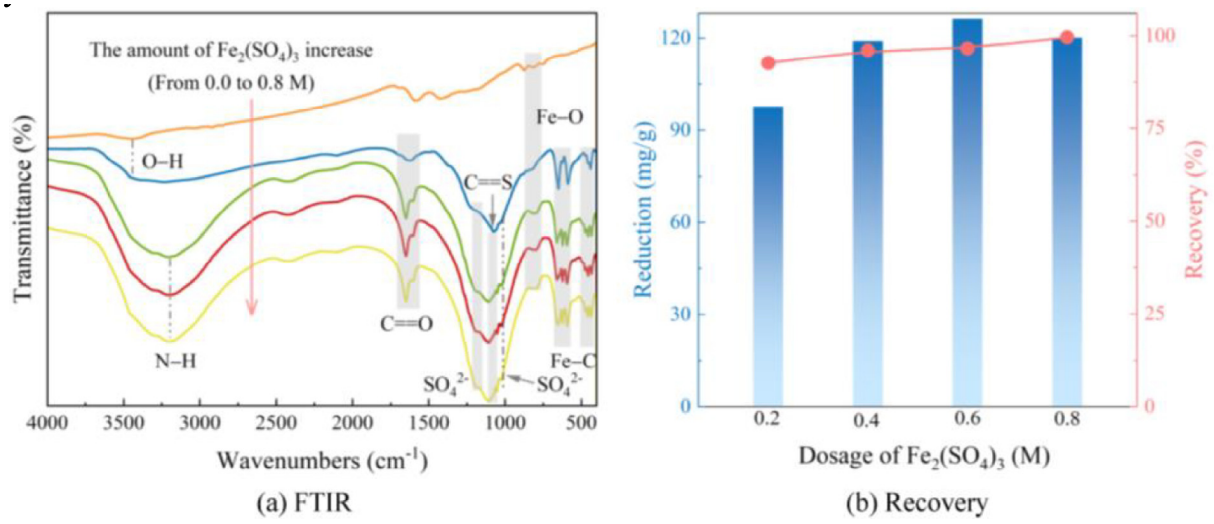

Fig. 12. FTIR spectra, electrochemical reduction-recovery performances of various $Fe_2(SO_4)_3$ dosages modified WSC electrodes.

emerge at ~796 and 610 cm^{-1} associated with ν_3 (SO_4^{2-}) vibrations [48]. The vibrational peak around 485 cm^{-1} corresponds to Fe—C, indicating the bonding between Fe and WSC. These results confirm the formation of $Fe_2(SO_4)_3$ after modifications. From the FTIR spectra of WSC modified with different $Fe_2(SO_4)_3$ concentrations, a noticeable redshift was observed as the $Fe_2(SO_4)_3$ concentration increased. This shift may be attributed to the strengthened interactions between $Fe_2(SO_4)_3$ and the molecular structure of WSC, leading to a decrease in bond vibration frequency.

As for the recovery of gold(I) using WSC modified with different $Fe_2(SO_4)_3$ concentrations, the results are shown in Fig. 12b. When the $Fe_2(SO_4)_3$ concentration used for modification was 0.2 M, the recovery of $Au(S_2O_3)_2^{3-}$ increased significantly. With further increases in the $Fe_2(SO_4)_3$ concentration, the recovery continued

to improve and then declined a little, indicating that excessive $Fe_2(SO_4)_3$ doping does not contribute significantly to further performance enhancement. To assess the material's stability, AAS was used to analyze the iron concentration in all post-reaction solutions. The results demonstrated that there was almost no iron leaching into the solution, confirming the stability of the modified material.

The electrochemical performances of WSC modified with different concentrations of $Fe_2(SO_4)_3$ was evaluated. Except for the modified WSC in Fig. 10a, the CV curves of WSC modified with different $Fe_2(SO_4)_3$ concentrations in the gold(I) solution system are shown in Fig. S3. All curves exhibit reduction peaks, confirming the reduction of gold(I) to metallic gold during the recovery process. With the aim of analyzing the capacitive reduction performances, the specific capacitance (C, F/g) of electrodes was calculated using CV by integrating the discharge current, as expressed in Eq. (3):

$$C = \frac{\int IdV}{2m\upsilon\Delta V} \tag{3}$$

where I represents the discharge current, A; m the loading mass of active material on the working electrode, g; υ the scan rate, mV/s; and ΔV the applied potential window, V.

The specific capacitive performances are shown in Fig. 13a. As the $Fe_2(SO_4)_3$ concentration increased, the specific capacitance initially increased and then decreased, reaching its peak at 0.4 M. This indicates that excessive $Fe_2(SO_4)_3$ adding may alter the pore structure or interfere with the intrinsic active sites of WSC. Similarly, an appropriate $Fe_2(SO_4)_3$ concentration reduced the charge transfer resistance (Figs. S4 and 13b), facilitating the electrochemical reduction-recovery of gold(I).

3.7. Effect of various ferric sources on gold(I) recovery

To investigate the impact of $Fe_2(SO_4)_3$ adding on electrochemical reduction-recovery of gold(I), we examined various ferric sources ($Fe(NO_3)_3$ and $FeCl_3$) to determine whether iron ions play a role in the process. Fig. 14a presents the XRD patterns of WSC modified with $Fe(NO_3)_3$ and $FeCl_3$. $FeCl_3$-WSC retained characteristic peaks corresponding to $FeCl_3$, whereas the $Fe(NO_3)_3$-WSC exhibited almost no identifiable peaks related to $Fe(NO_3)_3$. The peaks at ~16.0°, 20.8°, 32.6°, 35.6°, and 55.9° correspond to the (0 0 3), (0 1 2), (1 1 3), (0 2 1), and (1 0 1 0) crystal planes of $FeCl_3$, respectively. This suggests that $Fe(NO_3)_3$ is incorporated into WSC primarily as doped iron rather that a distinct phase. FTIR analysis (Fig. 14b) further supports this distinction. Apart from the fundamental vibrational peaks of WSC, the peaks at ~709 and 1347 cm^{-1} in $Fe(NO_3)_3$-WSC confirm the presence of NO_3^-, corresponding to the in-plane bending vibration (ν_4) and symmetric stretching vibration (ν_1) of NO_3^-, respectively. Additionally, the vibrational peak at 485 cm^{-1} observed in both $FeCl_3$-WSC and $Fe(NO_3)_3$-WSC is attributed to Fe—C vibrations, indicating the interaction between iron ions and WSC.

Fig. 15 shows the gold(I) recovery performance of WSC modified with $FeCl_3$ and $Fe(NO_3)_3$. The gold(I) reduction capacity and recovery of $FeCl_3$-WSC electrodes were both higher than those of $Fe(NO_3)_3$-WSC and WSC electrodes. In contrast, the gold(I) reduction capacity and recovery of $Fe(NO_3)_3$-WSC electrodes were similar to those of WSC electrodes, likely due to iron ions occupying the active sites within WSC, thereby reducing the material's effectiveness for gold(I) recovery. Oppositely, $FeCl_3$ and $Fe_2(SO_4)_3$ interact more synergistically with WSC, enhancing its performance. In comparison with state-of-the-art Pt electrocatalysts (Fig. S5), the electrode exhibits a remarkable improvement in catalytic efficiency.

Subsequently, the electrochemical performances of $FeCl_3$-WSC and $Fe(NO_3)_3$-WSC electrodes in Na_2SO_4 solutions were evaluated using CV and EIS tests. CV curves for all electrodes, including WSC, $Fe_2(SO_4)_3$-WSC, $FeCl_3$-WSC, and $Fe(NO_3)_3$-WSC electrodes were recorded at various scan rates (Figs. S6–S9), demonstrating that a well-maintained rectangular shape was preserved even at high scan rates. To understand the impact of modification on WSC electrodes, specific capacities were calculated (Fig. 16a). It was found that a significant improvement in specific capacities for $Fe_2(SO_4)_3$-WSC and $FeCl_3$-WSC electrodes, whereas $Fe(NO_3)_3$-WSC electrodes exhibited only a slight enhancement. Moreover, charge-transfer resistances were derived from Fig. S10 and 10d. As shown in Fig. 16b, Fe modification effectively reduced charge-transfer resistance. However, specific capacitance plays a more crucial role in the electrochemical reduction-recovery of gold(I).

Based on these findings, the recovery of gold(I) using different Fe(III)-modified WSC materials is primarily influenced by their interaction with WSC. $Fe_2(SO_4)_3$ and $FeCl_3$ modifications likely result in the formation of stable deposits or surface coatings, which enhance conductivity and improve the electrochemical activities for gold(I) recovery. In contrast, $Fe(NO_3)_3$-WSC primarily introduces Fe^{3+} dopants rather than forming stable compounds. This doping effect may disrupt the porous structure or reduce the availability of active Fe sites on the surface, ultimately leading to a lower gold(I) recovery.

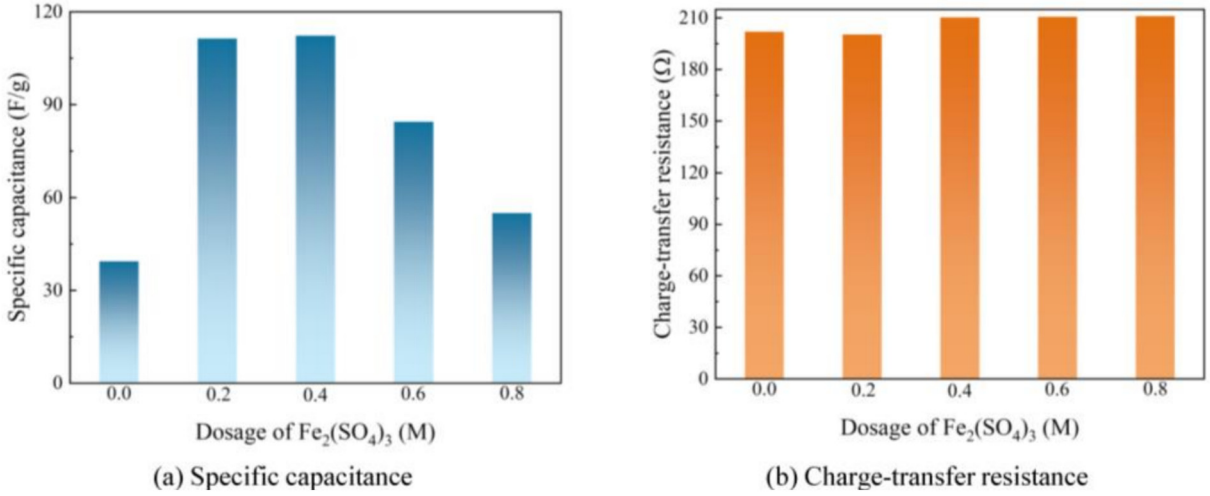

Fig. 13. Specific capacitance, and charge-transfer resistance of various $Fe_2(SO_4)_3$ dosages modified WSC electrodes.

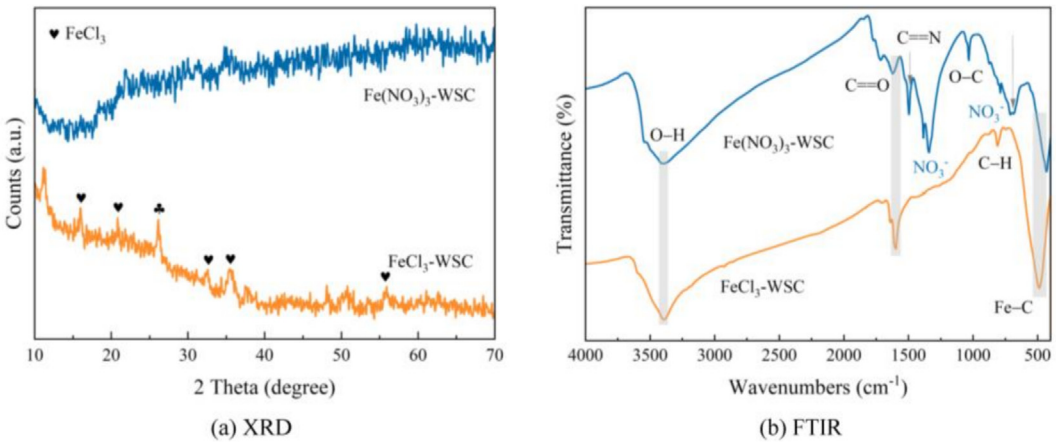

Fig. 14. XRD patters and FTIR spectra of $Fe(NO_3)_3$ and $FeCl_3$ modified WSC electrodes.

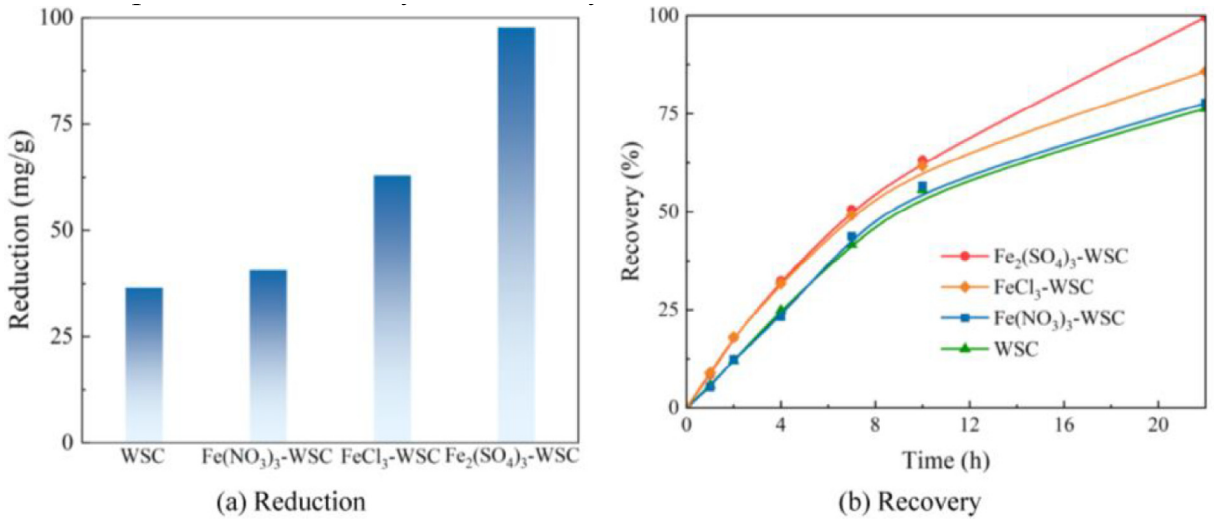

Fig. 15. Reduction capacity and recovery of gold(I) by $Fe(NO_3)_3$-WSC and $FeCl_3$-WSC electrodes.

3.8. Simulations for gold(I) interactions with various ferric sources

To explore the interactions between gold(I) and different ferric resources, including $Fe_2(SO_4)_3$, $FeCl_3$, and $Fe(NO_3)_3$, DFT calculations were conducted. As shown in the electron density maps (Fig. 17a), substantial charge accumulation was observed at the gold(I) interaction sites with $Fe_2(SO_4)_3$ and $FeCl_3$, including strong chemical interactions, explaining the O 1*s* and 2*p* shifts observed in XPS. In contrast, little to no charge redistribution occurred in the gold(I)-$Fe(NO_3)_3$ system, suggesting weak interaction in that case. To further quantify these interactions, adsorption energies were calculated (Fig. 17b). $Fe_2(SO_4)_3$ exhibited the strongest adsorption affinity for gold(I), which may be attributed to the presence of oxygen-containing functional groups that enhance binding strength. This trend was further supported by the Mulliken charge transfer (ΔQ) analysis (Fig. 17c), where $Fe_2(SO_4)_3$ and $FeCl_3$ showed more pronounced electro exchange with gold(I) compared to $Fe(NO_3)_3$. Additionally, partial density of states (PDOS) analysis (Fig. 17d) revealed significant orbital overlap between A_d and A_p orbitals with O_s and O_p orbitals, particularly in the $Fe_2(SO_4)_3$-modified system. This orbital hybridization further confirms the strong electronic coupling and facilitates the efficient interaction between gold(I) and the functionalized carbon surface. Although the ultimate recovery involves a reduction to metallic gold in XPS, the DFT results demonstrate that $Au(S_2O_3)_2^{3-}$ modification provides the most energetically favorable sites for the initial adsorption and subsequent electronic activation of gold complex. This strong "pre-concentration" effect facilitates the proximity of $Au(S_2O_3)_2^{3-}$ to the active Fe—C centers, thereby lowering the charge transfer resistance observed in electrochemical tests.

4. Conclusions

In this study, WSC electrodes modified with various ferric compounds were developed for the electrochemical reduction-recovery of trace gold(I) from thiosulfate solutions. Among the different ferric precursors evaluated, $Fe_2(SO_4)_3$ modified WSC exhibited the most outstanding performance, achieving near-complete recovery of trace gold(I) under optimized electrochemical conditions. The modification led to the formation of stable surface coatings and oxygen-rich functional groups, which enhanced electrical conductivity, increased specific capacitance, and reduced charge transfer resistance. Systematic investigations into the effects of modification dosage, solution parameters, and electrochemical

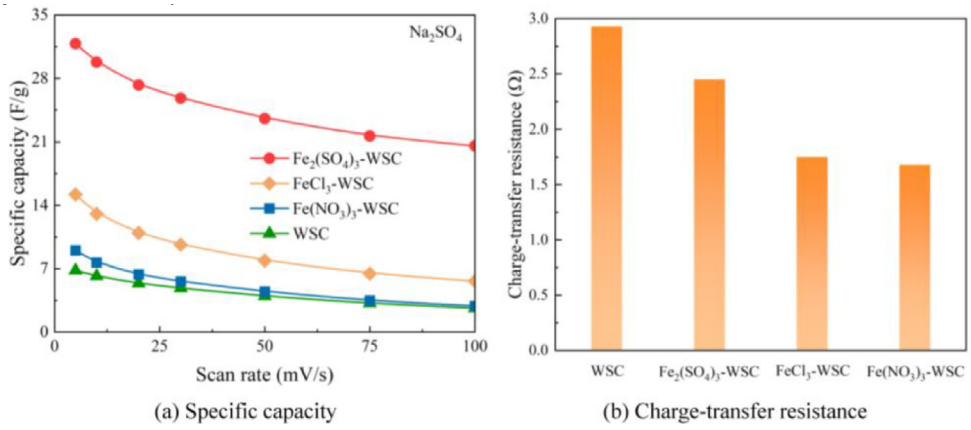

Fig. 16. Specific capacitance and charge-transfer resistance of various Fe sources modified WSC electrodes.

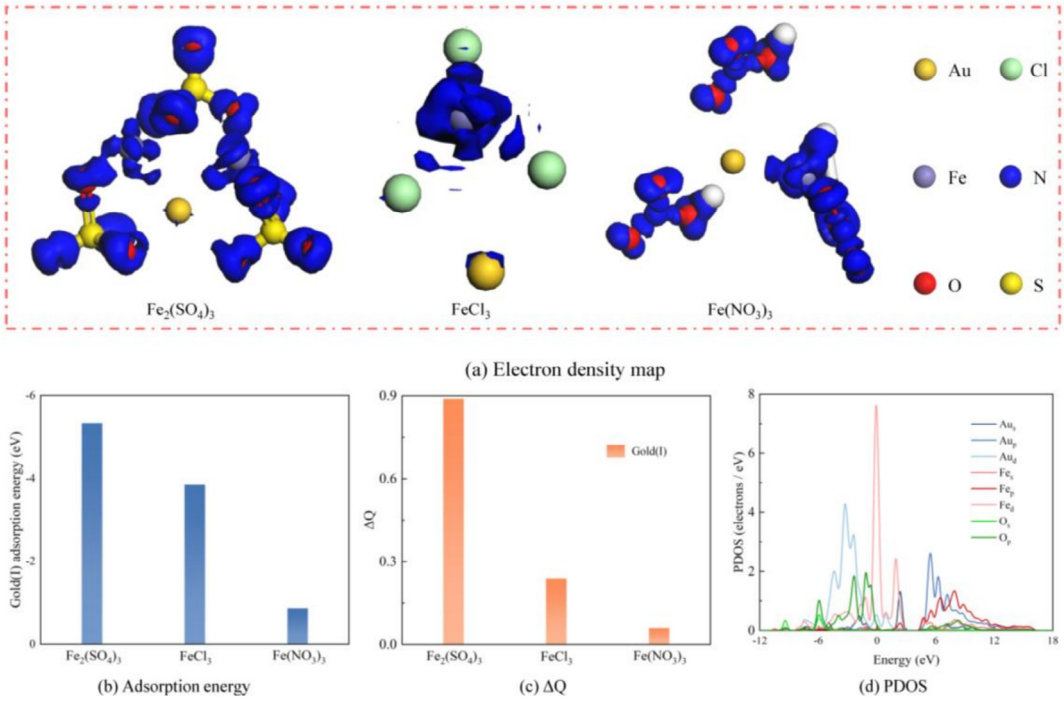

Fig. 17. Electron density map, adsorption energy, ΔQ, and PDOS analysis in the interactions of gold(I) with $Fe_2(SO_4)_3$, $FeCl_3$, and $Fe(NO_3)_3$.

conditions confirmed the critical role of sulfate groups induced by $Fe_2(SO_4)_3$. These groups significantly improved the adsorption affinity for gold(I), facilitating its pre-concentration near active sites and thus promoting efficient recovery. Complementary DFT simulations further revealed strong interactions between sulfate-derived oxygen atoms and gold(I), reinforcing the experimental findings. In contrast, $FeCl_3$-WSC electrodes also showed moderate recovery performance due to chloride-gold(I) coordination, while $Fe(NO_3)_3$-WSC electrodes demonstrated negligible enhancement. Collectively, these results emphasize the importance of ferric precursor selection in tuning the surface chemistry and electrochemical properties of carbon-based electrodes.

CRediT authorship contribution statement

Shaoxian Song: Writing – original draft, Formal analysis. **Weiquan Zhan:** Writing – review & editing, Writing – original draft, Formal analysis. **Qizheng Weng:** Investigation, Formal analysis. **Chun Zhan:** Validation, Methodology. **Feifei Jia:** Visualization.

Declaration of competing interest

The authors declare that they have no known competing financial interests or personal relationships that could have appeared to influence the work reported in this paper.

Acknowledgements

The work is financially supported by the National Natural Science Foundation of China (No. 52422406) through Excellent Young Scientists Fund.

Supplementary material

Supplementary data to this article can be found online at https://doi.org/10.1016/j.ijmst.2026.02.005.

References

[1] Yue CL, Sun HM, Liu WJ, Guan BB, Deng XD, Zhang X, et al. Environmentally benign, rapid, and selective extraction of gold from ores and waste electronic materials. Angew Chem Int Ed 2017;56(32):9331–5.
[2] Botero YL, Demers I, Cisternas LA, Avila A, Benzaazoua M. A cleaner production strategy for acid mine drainage prevention of waste rock: a porphyry copper case. Int J Min Sci Technol 2024;34(8):1163–77.
[3] Sun D, Gasilova N, Yang SL, Oveisi E, Queen WL. Rapid, selective extraction of trace amounts of gold from complex water mixtures with a metal–organic framework (MOF)/polymer composite. J Am Chem Soc 2018;140(48):16697–703.
[4] Papaiconomou N, Vite G, Goujon N, Lévêque JM, Billard I. Efficient removal of gold complexes from water by precipitation or liquid–liquid extraction using ionic liquids. Green Chem 2012;14(7):2050–6.
[5] Zhang YL, Li HM, Yu XJ. Recovery of iron from cyanide tailings with reduction roasting–water leaching followed by magnetic separation. J Hazard Mater 2012;213:167–74.
[6] Faraz S, Hossna D, Rezgar B, Piroz Z. Improved recovery of a low-grade refractory gold ore using flotation–preoxidation–cyanidation methods. Int J Min Sci Technol 2014;24(4):537–42.
[7] Brüger A, Fafilek G, Restrepo BOJ, Rojas-Mendoza L. On the volatilisation and decomposition of cyanide contaminations from gold mining. Sci Total Environ 2018;627:1167–73.
[8] Ahtiainen R, Lundström M. Cyanide-free gold leaching in exceptionally mild chloride solutions. J Clean Prod 2019;234:9–17.
[9] Liu C, Zhang H, Wang QH, Wu J, Chen P, Song SX, et al. Efficient gold recovery from low concentrated $Au(S_2O_3)_2^{3-}$ solution through enhanced photocatalysis via photothermal and surface plasmon resonance assistance on MoS_2/MXene/Ag. Desalination 2024;584:117733.
[10] Wang J, Wang W, Dong KW, Fu Y, Xie F. Research on leaching of carbonaceous gold ore with copper-ammonia-thiosulfate solutions. Miner Eng 2019;137:232–40.
[11] Zhan WQ, Yuan Y, Yang BQ, Jia FF, Song SX. Construction of MoS_2 nano-heterojunction via ZnS doping for enhancing in-situ photocatalytic reduction of gold thiosulfate complex. Chem Eng J 2020;394:124866.
[12] Gao JB, Zhan WQ, Xiang ZW, Song SX, Arauz-Lara JL, Jia FF, et al. Facet engineering in cadmium sulfide for efficient reduction-recovery of low-concentration gold(I) from thiosulfate solutions. J Mol Liq 2024;413:126018.
[13] Chen P, Ni JM, Liang YM, Yang BQ, Jia FF, Song SX. Piezo-photocatalytic reduction of Au(I) by defect-rich MoS_2 nanoflowers for efficient gold recovery from a thiosulfate solution. ACS Sustain Chem Eng 2021;9(1):589–98.
[14] Cook NJ, Ciobanu CL, Meria D, Silcock D, Wade B. Arsenopyrite-pyrite association in an orogenic gold ore: Tracing mineralization history from textures and trace elements. Econ Geol 2013;108(6):1273–83.
[15] Jeffrey MI, Hewitt DM, Dai X, Brunt SD. Ion exchange adsorption and elution for recovering gold thiosulfate from leach solutions. Hydrometall 2010;100(3–4):136–43.
[16] Dong ZL, Jiang T, Xu B, Li Q, Yang YB. Gold recovery from pregnant thiosulfate solution by ion exchange resin: Synergistic desorption behaviors and mechanisms. Sep Purif Technol 2023;323:124481.
[17] Grosse AC, Dicinoski GW, Shaw MJ, Haddad PR. Leaching and recovery of gold using ammoniacal thiosulfate leach liquors (a review). Hydrometall 2003;69(1–3):1–21.
[18] Yu H, Zi FT, Hu XZ, Nie YH, Chen YL, Cheng HL. Adsorption of gold from thiosulfate solutions with chemically modified activated carbon. Adsorpt Sci Technol 2018;36(1–2):408–28.
[19] Yu H, Zi FT, Hu XZ, Nie YH, Xiang PZ, Xu J, et al. Adsorption of the gold–thiosulfate complex ion onto cupric ferrocyanide (CuFC)-impregnated activated carbon in aqueous solutions. Hydrometall 2015;154:111–7.
[20] Chen Y, Zi F, Hu X, Lin Y, Du H, Hu J, et al. The first effective utilization of activated carbon in gold thiosulfate system: A more eco-friendly, easier method for gold recovery and material regeneration. Miner Eng 2020;155:106441.
[21] Dong ZL, Jiang T, Xu B, Wu JT, Li Q, Yang YB. A comparative study of electrodeposition and sodium dithionite reduction for recovering gold in gold-rich solution from the adsorption of thiosulfate solution by ion exchange resin. Sep Purif Technol 2024;328:125053.
[22] Weng QZ, Zhan WQ, Zhang X, Song SX, Zeng ZL, Lwin HM, et al. Electrochemical reduction and recovery of trace gold(I) from environmentally friendly thiosulfate leaching solutions using carbon electrodes. Carbon 2025;232:119799.
[23] Liu C, Li L, Zhang H, Wang QH, Liang YM, Chen P, et al. Efficient Au $(S_2O_3)_2^{3-}$recovery from $S_2O_3^{2-}$ system through coupling electromigration and photocatalysis effect on defect introduced and oxygen incorporated MoS_2. Sep Purif Technol 2025;363:132251.
[24] Zhang X, Zhan WQ, Weng QZ, Wang S, Song SX, Arauz-Lara JL, et al. Electro reduction-recovery of $Au(S_2O_3)_2^{3-}$ within a low concentration range via multi-porous activated carbon electrodes. Sep Purif Technol 2025;354:129134.
[25] McCreery RL. Advanced carbon electrode materials for molecular electrochemistry. Chem Rev 2008;108(7):2646–87.
[26] Yang XM, Xie D, Wang WH, Li SZ, Tang ZM, Dai SL. An activated carbon from walnut shell for dynamic capture of high concentration gaseous iodine. Chem Eng J 2023;454:140365.
[27] Zhuang ZT, Liu YB, Wei WW, Shi JW, Jin H. Preparation of biochar adsorption material from walnut shell by supercritical CO_2 pretreatment. Biochar 2024;6(1):11.
[28] Zhu KY, Ma J, Cong JZ, Zhang T, Lei HJ, Xu HD, et al. The road to reuse of walnut by-products: A comprehensive review of bioactive compounds, extraction and identification methods, biomedical and industrial applications. Trends Food Sci Technol 2024;143:104264.
[29] Weng QZ, Song SX, Zhan WQ, Zhang X, Xiang ZW, Gao JB, et al. Novel recovery of a low-concentration gold thiosulfate complex through electroreduction via a walnut shell charcoal electrode. Green Smart Min Eng 2024;1(1):58–66.
[30] Karousis N, Tagmatarchis N, Tasis D. Current progress on the chemical modification of carbon nanotubes. Chem Rev 2010;110(9):5366–97.
[31] Liang CD, Li ZJ, Dai S. Mesoporous carbon materials: Synthesis and modification. Angew Chem Int Ed 2008;47(20):3696–717.
[32] Faria PCC, Órfão JJM, Pereira MFR. Adsorption of anionic and cationic dyes on activated carbons with different surface chemistries. Water Res 2004;38(8):2043–52.
[33] Liu WF, Zhang J, Zhang CL, Ren L. Preparation and evaluation of activated carbon-based iron-containing adsorbents for enhanced Cr(VI) removal: Mechanism study. Chem Eng J 2012;189:295–302.
[34] Zhu YE, Li H, Zhang GX, Meng FJ, Li LF, Wu S. Removal of hexavalent chromium from aqueous solution by different surface-modified biochars: Acid washing, nanoscale zero-valent iron and ferric iron loading. Bioresour Technol 2018;261:142–50.
[35] Liang YM, Zhan WQ, Yuan Y, Zamora-Romero N, Jia FF, Yang BQ, et al. Manganese and oxygen dual-doping MoS_2 boosts reduction and adsorption activity toward efficient recovery of gold(I) from thiosulfate solutions. J Alloy Compd 2022;928:167185.
[36] Korolev I, Altinkaya P, Haapalainen M, Kolehmainen E, Yliniemi K, Lundström M. Electro-hydrometallurgical chloride process for selective gold recovery from refractory telluride gold ores: a mini-pilot study. Chem Eng J 2022;429:132283.
[37] Zhan WQ, Zhang X, Yuan Y, Weng QZ, Song SX, de Jesús M-López M, et al. Regulating chemisorption and electrosorption activity for efficient uptake of rare earth elements in low concentration on oxygen-doped molybdenum disulfide. ACS Nano 2024;18(9):7298–310.
[38] Chen SL, Yang YX, Zi FT, Hu XZ, Li XR. Constructing phosphine-containing microspheres for selective recovery of gold(I) thiosulfate complex by adjusting the interaction site. Sep Purif Technol 2025;362:131636.
[39] Zhan W. Rare and precious metal recovery at a low concentration via chemisorption and electrosorption coupling process. Repositorio Nacional Conacyt 2025.
[40] Yao JH, Jin TF, Li YW, Xiao SH, Huang B, Jiang JQ. Electrochemical performance of $Fe_2(SO_4)_3$ as a novel anode material for lithium-ion batteries. J Alloy Compd 2021;886:161238.
[41] Yao YH, Huang GX, Liu YB, Liu Y, Li YY, Han GX, et al. Facile synthesis of B/N Co-doped porous carbon nanosheets with high heteroatom content and electrical conductivity for excellent-performance supercapacitors. Appl Surf Sci 2022;580:152236.
[42] Wu X, Chen YL, Xing Z, Lam CWK, Pang SS, Zhang W, et al. Advanced carbon-based anodes for potassium-ion batteries. Adv Energy Mater 2019;9(21):1900343.
[43] Feng C, Han LP, Wang PL, Liu XY, Zhou GY, Zhang DS. Unraveling SO^{2-} tolerant mechanism over $Fe_2(SO_4)_3/TiO_2$ catalysts for NO_x reduction. J Environ Sci 2022;111:340–50.
[44] Wu B, Xiong YQ, Ge YY. Simultaneous removal of SO_2 and NO from flue gas with OH from the catalytic decomposition of gas-phase H_2O_2 over solid-phase $Fe_2(SO_4)_3$. Chem Eng J 2018;331:343–54.
[45] Grosvenor AP, Kobe BA, Biesinger MC, McIntyre NS. Investigation of multiplet splitting of Fe 2p XPS spectra and bonding in iron compounds. Surf Interface Anal 2004;36(12):1564–74.
[46] Zhan WQ, Yuan Y, Yao X, Yang BQ, Jia FF, Lin CS, et al. Efficient recovery of gold (I) from thiosulfate solutions through photocatalytic reduction with Mn(II)-doped MoS_2. ACS Sustain Chem Eng 2021;9(35):11681–90.
[47] Ran JC, Song ZY, He QQ, Miao ZY. Coal pitch-based nanosheets enhance the electronic and ionic transport of flow electrode capacitive deionization. Int J Min Sci Technol 2025;35(5):691–702.
[48] Ding HJ, Long YZ, Shen JY, Wan MX. $Fe_2(SO_4)_3$ as a binary oxidant and dopant to thin polyaniline nanowires with high conductivity. J Phys Chem B 2010;114(1):115–9.